A reduced model to simulate the damage in composite laminates under low velocity impact

S. Metoui [a,b,*], E. Pruliere [a], A. Ammar [b], F. Dau [b]

[a] Ecole Nationale Supérieure d'Arts et Métiers, Campus de Bordeaux, I2M-DuMAS, Esplanade des Arts et Métiers, Talence 33405, France
[b] Ecole Nationale Supérieure d'Arts et Métiers, Campus d'Angers, LAMPA, 2 Boulevard de Ronceray, 49035 Angers Cedex 01, France

ARTICLE INFO

Article history:
Received 14 April 2017
Accepted 21 January 2018

Keywords:
Composite materials
Model reduction
PGD
Impact
Damage

ABSTRACT

This article presents an efficient numerical strategy to simulate the damage in composite laminates under low velocity impact. The proposed method is based on a separated representation of the solution in the context of the Proper Generalized Decomposition (PGD). This representation leads to an important reduction of the number of degrees of freedom. In addition to the PGD, the main ingredients of the model are the following: (a) cohesive zone models (CZM) to represent the delamination and the matrix cracking, (b) a modified nonlinear Hertzian contact law to calculate the impact force, (c) the implicit Newmark integration scheme to compute the evolution of the solution during the impact. The method is applied to simulate an impact on a laminated plate. The results are similar to the solution obtained with a classical finite element simulation. The shape of the delaminated area is found to be coherent with some experimental results from the literature.

1. Introduction

The ever growing demand for lighter structures results in the increasing replacement of metallic materials by composite materials. While composite materials offer a number of superior design characteristics, composite structures are much more sensitive to impact damage than similar metallic structures. Impact can result in numerous damage mechanisms, ranging from barely visible impact damage (BVID) to complete penetration, which nevertheless severely reduces the stiffness and the residual strength of the composite structures. Impacts caused by foreign objects may arise during the life span of a structure including manufacturing, service, and maintenance operations. In the present work only low velocity impact events will be considered although the proposed numerical strategy may be applied to other kind of dynamic loads.

The development of efficient dynamic simulations for composite structures under low velocity impact is a very challenging issue. There are many scientific locks, in particular:

- Composite structures have often a small dimension (thickness) compared to the others (shell or plate structures). When using 3D elements, a fine mesh is required to keep a good precision in the thickness which results in a very high number of elements to cover the entire volume.
- The modeling of damages can also lead to numerical difficulties. For example, the use of cohesive elements is an appealing choice. This kind of elements is particularly well adapted to treat delamination and fibers/matrix decohesion. However, cohesive elements need very fine meshes to ensure the numerical stability.
- Explicit dynamic calculations lead to restrictive time steps to satisfy the stability condition. In the other hand, the use of implicit scheme causes solving some non linear problems many times which is numerically costly. The strong non-linearities related to the damage model are generally difficult to solve and require high computational resources.

The main objective of this work is to propose an efficient numerical solver able to simulate the complex behavior of composite laminates with reasonable computational time and accuracy. To reach this objective, an approach based on model reduction is chosen.

* Corresponding author at: Ecole Nationale Supérieure d'Arts et Métiers, Campus de Bordeaux, I2M-DuMAS, Esplanade des Arts et Métiers, Talence 33405, France.
E-mail addresses: sondes.metoui@ensam.eu (S. Metoui), Etienne.Pruliere@ensam.eu (E. Pruliere), amine.ammar@ensam.eu (A. Ammar), frederic.dau@ensam.eu (F. Dau).

https://doi.org/10.1016/j.compstruc.2018.01.012

1.1. Model reduction

The idea is to approximate the solution under a separated form. If we consider a plate structure where z is the coordinate in the direction normal to the plate, an unknown field (the displacement in general) can be expressed with the following separated representation:

$$u(x,y,z) = \sum_{i=1}^{n} F_i(x,y) \times G_i(z) \tag{1}$$

where the functions F_i and G_i for $i = 1,\ldots,n$ need to be determined. A few solvers exist to compute this kind of solution. Here, the Proper Generalized Decomposition (PGD) will be considered.

This numerical method consists in building the separated representation of the solution using a greedy algorithm with no a priori knowledge of any reduced basis. If n is small enough, the total number of degrees of freedom is significantly reduced. Only a 2D mesh is required and the problem is greatly simplified in comparison to the full 3D approach.

The PGD with a space-time separated representation was originally proposed by Ladeveze under the name "radial loading decomposition" in the context of the LATIN method. The idea was to develop a non-incremental solver [1,2]. Ammar et al. [3,4] devised the first version of the PGD strategy for multi-dimensional problems. It was originally applied to the high-dimensional kinetic models of complex fluids. After that, the PGD was successfully applied to a wide variety of problems. For instance, the PGD procedure was applied by Ammar et al. [5] to model the degradation of a plastic material which is a complex transient problem. A separated representation was also used by Chinesta et al. for solving the chemical master equation [6] and stochastic equations within the Brownian configuration field framework [7]. The PGD was applied in other studies for thermal problems in composite materials [8]. Nouy used the PGD to study stochastic problems [9,10]. This approach also allows for the fast computation of problems defined in plate or shell domains. The advantage is that 3D solutions can be obtained with a computational cost characteristic of standard 2D solutions [11]. This approach has been applied to composites shell structures [12] and have been improved using high order interpolation in the thickness [13,14]. In this work the PGD will be adapted to simulate a low velocity impact on a composite laminate involving damages.

1.2. Failure mechanisms in low velocity impact

Low velocity impact damage in composites is insidious due to the invisible damages they can cause. These damages can drastically decrease the residual strength of composite structure, for instance in compression after impact. For unidirectional (UD) laminates under low velocity impact, significant amount of permanent damage in the form of matrix cracking, delaminations and fiber breakage may be present without being detectable by visual inspection. The failure mechanisms usually occur in the listed order with increasing impact energy. Matrix cracking has been widely reported as the first type of failure induced by transverse low velocity impact [15–17]. It acts as a starting point for the propagation of delamination. Fig. 1 shows the typical matrix cracking and delamination damage found in an impacted composite specimen. Matrix cracks appear parallel to the fibers due to tension or shear.

The initiation and propagation of matrix cracks are strongly dependent on the stacking sequence [18–20]. Two types of matrix cracking can be observed: tensile matrix cracks and shear matrix cracks. Tensile matrix cracks are formed by the flexural deformations due to the tensile bending stresses. These cracks are generally located at the lower plies. Shear matrix cracks form in the upper plies directly under the impact zone and are induced by the high transverse shear stress through the material, and are inclined at approximately 45°. The matrix cracks first appear in the lowest ply [21]. Due to the coupling between delamination and matrix cracking, the initiation of delamination is located on the matrix cracks.

Delamination is often considered to be the most energy consuming damage mechanism during a low velocity impact. The majority of the energy absorbed in the laminate during impact dissipates into delamination propagation. Delaminations occur at the interfaces between plies with different fiber orientations and tend to initiate at the bottom interface and progressively becomes smaller towards the impact face. The shape of the delaminated area changes with the orientation of plies and is usually a peanut with its major axis oriented in the fiber direction of the lowermost layer at the interface, as depicted in Fig. 2. The peanut shape is a result of the shear stress distribution around the impactor, the interlaminar shear strength in the fiber direction and the matrix cracking. Fiber failure mostly appears after matrix cracking and delamination. This failure mode may occur under the impactor due to locally high stresses and indentation effects.

2. Problem statement

2.1. Governing equation

The weak form of the equilibrium equation in a domain Ω without body force and neglecting the damping effects reads:

$$\iint_{\Omega} \rho \mathbf{u}^* \cdot \ddot{\mathbf{u}} d\Omega + \iint_{\Omega} \varepsilon(\mathbf{u}^*) \cdot (\boldsymbol{A}\varepsilon(\mathbf{u})) d\Omega = \int_{\Gamma} \mathbf{T}_{ext} \mathbf{u}^* d\Gamma \tag{2}$$

where $\mathbf{u} = (u,v,w)^T$ is the displacement field, $\ddot{\mathbf{u}} = (\ddot{u},\ddot{v},\ddot{w})^T$ is the acceleration field, $\mathbf{u}^*$ is the virtual displacement and $\boldsymbol{\varepsilon}$ is the strain tensor using the vectorial form:

$$\boldsymbol{\varepsilon} = \begin{pmatrix} \varepsilon_{xx} \\ \varepsilon_{yy} \\ \varepsilon_{zz} \\ 2\varepsilon_{yz} \\ 2\varepsilon_{xz} \\ 2\varepsilon_{xy} \end{pmatrix} \tag{3}$$

$\mathbf{T}_{ext}$ is the external force on the boundary Γ. $\mathbf{A}$ is a matrix related to the material law in each layer. For a linear orthotropic material, $\mathbf{A}$ is defined by Eq. (4).

$$\boldsymbol{A}^{-1} = \begin{bmatrix} \frac{1}{E_x} & -\frac{\nu_{xy}}{E_x} & -\frac{\nu_{xz}}{E_x} & 0 & 0 & 0 \\ -\frac{\nu_{xy}}{E_x} & \frac{1}{E_y} & -\frac{\nu_{yz}}{E_y} & 0 & 0 & 0 \\ -\frac{\nu_{xz}}{E_x} & -\frac{\nu_{yz}}{E_y} & \frac{1}{E_z} & 0 & 0 & 0 \\ 0 & 0 & 0 & \frac{1}{G_{xz}} & 0 & 0 \\ 0 & 0 & 0 & 0 & \frac{1}{G_{xz}} & 0 \\ 0 & 0 & 0 & 0 & 0 & \frac{1}{G_{xz}} \end{bmatrix} \tag{4}$$

E_x, E_y, E_z are the elastic modulus, ν_{xy}, ν_{xz}, ν_{yz} are the Poission's ratio and G_{xy}, G_{xz}, G_{yz} are the shear modulus expressed in the orthotropic basis (x,y,z).

After assembling all mass and stiffness matrices with a finite element approximation, the discretized motion equations of the laminate take the following form:

$$[\mathbf{M}]\{\ddot{\mathbf{u}}\} + [\mathbf{K}]\{\mathbf{u}\} = \{F\} \tag{5}$$

where $[\mathbf{M}]$ and $[\mathbf{K}]$ are the coherent mass and stiffness matrices of the composite laminate, $\{\mathbf{u}\}$ and $\{\ddot{\mathbf{u}}\}$ are respectively the nodal

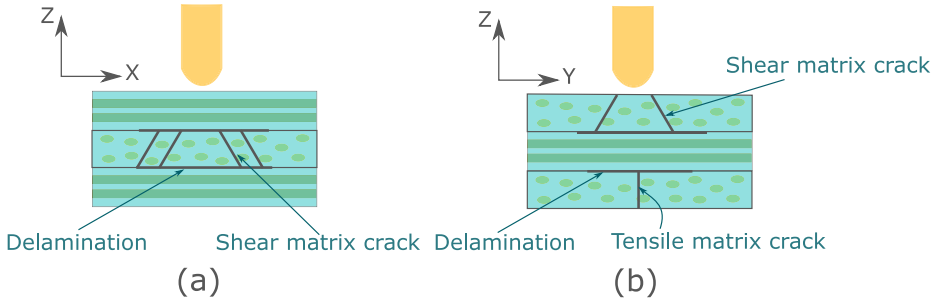

Fig. 1. Typical matrix cracking and delamination damage in a [0/90/0] UD laminated composite (a- longitudinal view, b- transverse view).

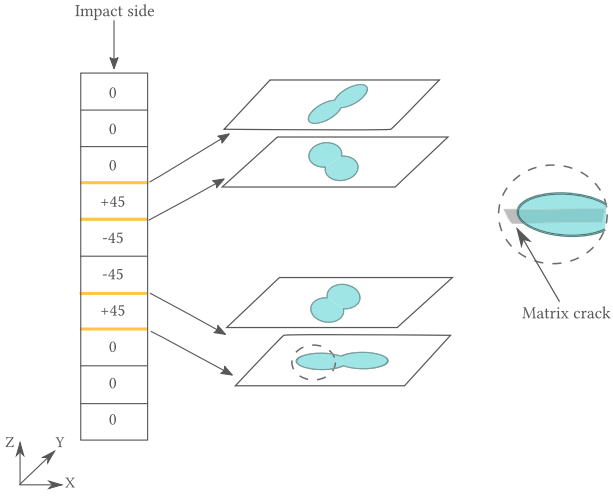

Fig. 2. Shape of the delamination.

displacement and acceleration vectors. In the following $\{g\}$ denotes the column vector containing the nodal values of any function g.

$\{F\}$ is the external force vector. For a low velocity impact, $\{F\}$ contains the impact force between the impactor and the plate:

$$\{F\} = \{0\ 0\ 0 \ldots F_c \ldots 0\ 0\ 0\}^T \tag{6}$$

where F_c is the contact force supposed to be concentrated on a single node. In general, the magnitude of the contact force is not known a priori and needs to be calculated using a contact law.

2.2. Time integration

There are many methods to solve Eq. (5) in time. In the present work the solution of the problem is determined by applying the implicit Newmark's integration scheme [22]. The time dimension is divided into time increments Δt. The system is then solved incrementally.

Eq. (5) can be written at time $t + \Delta t$ as:

$$[\mathbf{M}]\{\ddot{\mathbf{u}}_{t+\Delta t}\} + [\mathbf{K}]\{\mathbf{u}_{t+\Delta t}\} = \{F_{t+\Delta t}\} \tag{7}$$

The acceleration and velocity vectors at time $t + \Delta t$ are expressed as:

$$\{\ddot{\mathbf{u}}_{t+\Delta t}\} = \frac{1}{\beta(\Delta t)^2}[\{\mathbf{u}_{t+\Delta t}\} - \{\mathbf{u}_t\} - (\Delta t)\{\dot{\mathbf{u}}_t\}] - \frac{1}{\beta}\left(\frac{1}{2} - \beta\right)\{\ddot{\mathbf{u}}_t\} \tag{8}$$

$$\{\dot{\mathbf{u}}_{t+\Delta t}\} = \{\dot{\mathbf{u}}_t\} + (\Delta t)[(1-\gamma)\{\ddot{\mathbf{u}}_t\} + \gamma\{\ddot{\mathbf{u}}_{t+\Delta t}\}] \tag{9}$$

β and γ are numerical parameters that allow to control both the stability and the amount of numerical damping introduced into the system by the method. For $\gamma = \frac{1}{2}$ there is no numerical damping, for $\gamma \geqslant \frac{1}{2}$ numerical damping is introduced.

Newmark method is unconditionally stable when $\frac{1}{2} \leqslant \gamma \leqslant 2\beta$ and it is unstable when $\gamma < \frac{1}{2}$.

To avoid numerical instability, high frequency dissipation is required. It is achieved when: $\beta = \frac{1}{4}(\gamma + \frac{1}{2})^2$.

In this work, the constant average acceleration version of Newmark method is used, which is implicit and unconditionally stable. Thus, γ is $\frac{1}{2}$ and β is $\frac{1}{4}$. Substituting Eq. (8) into Eq. (7), we obtain a set of nonlinear equations in which the unknowns are $\{\mathbf{u}_{t+\Delta t}\}$ and $\{F_{t+\Delta t}\}$. The terms at time (t) are all known. The new system can then be formulated as:

$$[\mathbf{K}^*]\{\mathbf{u}_{t+\Delta t}\} = \{F^*_{t+\Delta t}\} \tag{10}$$

where $[\mathbf{K}^*]$ is the effective stiffness matrix, and $\{F^*_{t+\Delta t}\}$ is the force vector, which are defined as:

$$[\mathbf{K}^*] = \left[[\mathbf{K}] + \frac{1}{\beta(\Delta t)^2}[\mathbf{M}]\right] \tag{11}$$

$$\{F^*_{t+\Delta t}\} = \{F_{t+\Delta t}\} + [\mathbf{M}]\left\{\frac{1}{\beta(\Delta t)^2}\{\mathbf{u}_t\} + \frac{1}{\beta(\Delta t)}\{\dot{\mathbf{u}}_t\} + \left(\frac{1}{2\beta} - 1\right)\{\ddot{\mathbf{u}}_t\}\right\} \tag{12}$$

The calculation of $\{F_{t+\Delta t}\}$ will be detailed in the next section.

2.3. Calculation of the contact force

As indicated by Trousset [23], during finite element simulations of low velocity impact, about 90% of the total computation time is spent in the contact treatment. To avoid contact management during the impact simulation, the Hertzian contact law is commonly employed to deal with the contact between the impactor and the laminate.

Various researchers have developed finite element models in conjunction with the Hertzian contact law to study the impact response of laminated composite plates. Some important works on this subject can be found in Refs. [24–29].

In the present work, the contact force is calculated using a modified nonlinear Hertzian contact law proposed by Tan and Sun [24]. The impactor is hemispherical with isotropic properties: Young's modulus E_i, Poisson's ratio ν_i, radius R_i and mass m_i. The stiffness of the impactor is assumed to be higher than the one of the composite plate in the direction of impact. The initial velocity and displacement of the impactor are $\dot{w}_i = V_0$ and $w_i = 0$. The dynamic equation of the impactor is obtained through Newton's second law, where $\ddot{w}_i$ is the acceleration of the impactor:

$$m_i\ddot{w}_i = -F_c \tag{13}$$

In this model, an interpenetration between the plate and the impactor is possible which corresponds to a local indentation of the plate by the impactor. The local identation α is defined as the difference between the displacement of the impactor $w_i(t)$ and the deflection of the plate at the contact point $w_p(t)$:

$$\alpha(t) = w_i(t) - w_p(t) \tag{14}$$

The contact force F_c is related to the local indentation α according to a contact law (Fig. 3).

During the loading and unloading, the contact force is expressed as follows:

$$F_c = \begin{cases} k\alpha^{3/2} & \textit{loading} \\ F_m\left(\frac{\alpha-\alpha_0}{\alpha_m-\alpha_0}\right)^{5/2} & \textit{unloading} \end{cases} \tag{15}$$

where F_m is the maximum contact force at the beginning of unloading, α_m is the indentation corresponding to F_m. For laminated plate with orthotropic layers, the modified Hertz constant stiffness k can be calculated as [24]:

$$k = \frac{4}{3}\frac{\sqrt{R_i}}{\left(\frac{1-\nu_i^2}{E_i}+\frac{1}{E_z}\right)} \tag{16}$$

where E_z is the transverse modulus normal to the fiber direction in the uppermost composite layer. The permanent indentation α_0 is zero when the maximum indentation α_m is less than a critical value α_{cr}, otherwise α_0 is expressed as:

$$\alpha_0 = \begin{cases} 0 & \alpha_m < \alpha_{cr} \\ \alpha_m\left[1-\left(\frac{\alpha_{cr}}{\alpha_m}\right)^{2/5}\right] & \alpha_m \geqslant \alpha_{cr} \end{cases} \tag{17}$$

The velocity $\dot{w}_i^{n+1}$ and displacement w_i^{n+1} of the impactor at the time step $n+1$ are determined by applying the implicit Newmark's integration scheme described on Section 2.2 ($\gamma = \frac{1}{2}$ and $\beta = \frac{1}{4}$):

$$\dot{w}_i^{n+1} = \dot{w}_i^n + \ddot{w}_i^n\left(\frac{\Delta t}{2}\right) - F_c^{n+1}\left(\frac{\Delta t}{2m_i}\right) \tag{18}$$

$$w_i^{n+1} = w_i^n + \dot{w}_i^n\Delta t + \ddot{w}_i^n\left(\frac{\Delta t^2}{4}\right) - F_c^{n+1}\left(\frac{\Delta t^2}{4m_i}\right) \tag{19}$$

Hertz's law is applied at each time step to calculate the contact force. The contact force at time step $n+1$ is calculated from the impactor and plate displacements of the previous time step n. Substituting Eq. (19) into Eq. (15), we obtain the contact force at time step $n+1$:

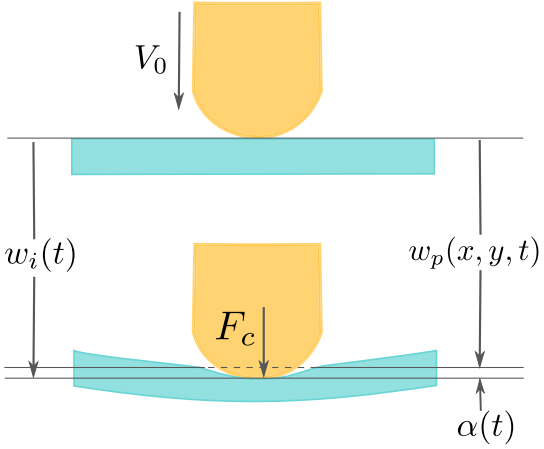

Fig. 3. Schematic Illustration of the impact procedure.

$$F_c^{n+1} = \begin{cases} k\left[q - w_p^{n+1} - \left(\frac{\Delta t^2}{4m_i}\right)F_c^{n+1}\right]^{3/2} & \text{loading} \\ \frac{F_m}{(\alpha_m-\alpha_0)^{5/2}}\left[q - w_p^{n+1} - \alpha_0 - \left(\frac{\Delta t^2}{4m_i}\right)F_c^{n+1}\right]^{5/2} & \text{unloading} \end{cases} \tag{20}$$

where $q = w_i^n + \dot{w}_i^n\Delta t + \ddot{w}_i^n\left(\frac{\Delta t^2}{4}\right)$.

To seek the solution of the nonlinear problem defined in Eq. (20), the Newton-Raphson iteration technique is adopted. Using the initial conditions ($\dot{w}_i = V_0$ and $w_i = w_p = 0$) and a root finding algorithm (Newton-Raphson method), an approximate value of the impact force F_c is obtained from the implicit expressions of the modified nonlinear Hertzian contact law (the first equation of Eq. (20)). This force is now applied as external load at the contact point of the plate. The nodal displacement w_p of the laminated plate is next found from Eq. (10). Using this value of w_p, the impact force F_c is recomputed from Eq. (20). The process is repeated until the required accuracy is achieved. The convergence criteria for the satisfaction of the local equilibrium related to the contact force is:

$$|F_c^{n+1}| - |F_c^n| \leqslant 1.0\times10^{-6} \tag{21}$$

The contact force is then used to calculate acceleration, velocity, and displacement of the impactor for the next time step.

2.4. Damage modeling

Several models based on the fracture mechanics are used in the literature to predict the damage evolution in composites. For instance, the virtual crack closure technique (VCCT) is widely considered [30]. In this work, the modeling of damages is based on a cohesive zone model which has the advantage to account at the same time for the initiation and the propagation of a crack. This model is well adapted when the crack path is known a priori, for instance when considering interface damages like delaminations. Cohesive zone models required the definition of a cohesive law that describe the behavior of a predefined interface. Here, we choose the Crisfield law [31,32] shown in Fig. 4 which presents linear elastic and linear softening behavior. Three parameters are required to define the cohesive law for each pure mode: mode I (opening) and mode II (shear). These parameters are the maximum stress (σ_{Ic} and σ_{IIc}), the critical strain energy release rate (G_{Ic} and G_{IIc}) and the interface element stiffness (K_I and K_{II}).

The critical value of the energy release rate of the interface is equal to the area under the interfacial stress-separation curve. The critical separations (δ_c^I and δ_c^{II}) are defined when the interfacial stress reaches maximum, and the maximum separations (δ_m^I and δ_m^{II}) are defined when the stress becomes zero. These separations can be evaluated by the following expressions:

$$\delta_c^I = \frac{\sigma_{Ic}}{K_I},\ \delta_c^{II} = \frac{\sigma_{IIc}}{K_{II}} \tag{22}$$

$$\delta_m^I = \frac{2G_{Ic}}{\sigma_{Ic}},\ \delta_m^{II} = \frac{2G_{IIc}}{\sigma_{IIc}} \tag{23}$$

The relation between local separation (δ_I and δ_{II}) and interface stress (σ_I and σ_{II}), shown in Fig. 4, can be expressed as:

$$\sigma_i = \begin{cases} K_i\delta_i & \delta_i < \delta_c^i \\ (1-d_i)K_i\delta_i & \delta_c^i \leqslant \delta_i < \delta_m^i, \\ 0 & \delta_i \geqslant \delta_m^i \end{cases} \quad i = I, II \tag{24}$$

$$d_i = \frac{\delta_m^i(\delta_i - \delta_c^i)}{\delta_i(\delta_m^i - \delta_c^i)},\ i = I, II;\ d_i \in [0,1] \tag{25}$$

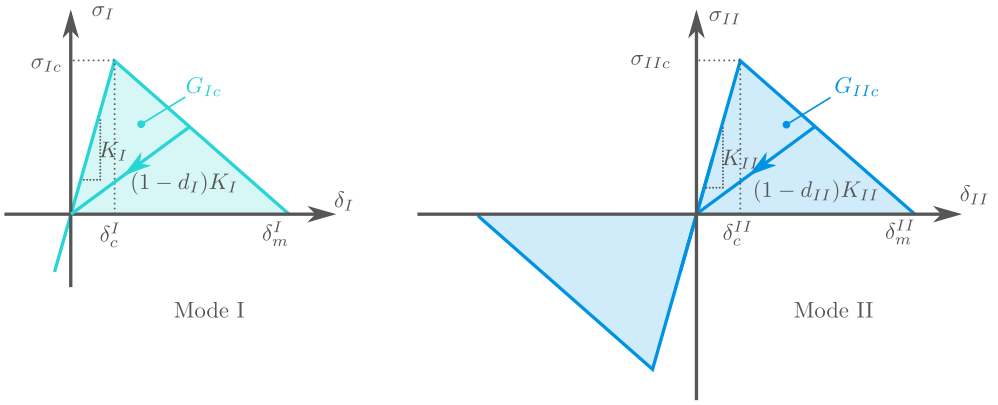

Fig. 4. Crisfield cohesive law for the mode I and mode II.

where d_i is the damage variable whose value evolves from 0 (undamaged) to 1 (full damaged).

The interface element stiffness (K_I and K_{II}) are purely numerical parameters. Their values are chosen by compromise considering than: (i) too high values lead to spurious stress oscillations, (ii) too low values lead to non physical behavior (discontinuity of the displacement in the undamaged state) [33].

The description of the cohesive law under mixed-mode loading requires: (i) the definition of the interfacial stress and the critical energy release rate for each pure mode and, (ii) the proposition of criteria or laws relating these parameters for mixed loading [34]. From these laws, the critical and maximum separations (δ_c^m and δ_m^m) under mixed-mode loading can be determined. Each failure mechanism consists of two parts: a damage initiation criterion and a damage evolution law.

The damage initiation can be predicted using the quadratic failure criterion, defined as:

$$\left(\frac{\langle\sigma_I\rangle_+}{\sigma_{Ic}}\right)^2+\left(\frac{\sigma_{II}}{\sigma_{IIc}}\right)^2=1 \tag{26}$$

$\langle\sigma_I\rangle_+$ denotes the positive value of σ_I (if σ_I<0, $\langle\sigma_I\rangle_+=0$).

This mixed-mode criterion assumes the coupling between the failure modes and considers that compressive normal stresses have no influence on the delamination onset.

The "power law criterion" appears to be the most reliable in order to predict delamination propagation in composite laminates carbone/epoxy under mixed-mode loading. It states that the damage under mixed loading is governed by a power law interaction between the energies of pure modes.

$$\left(\frac{G_I}{G_{Ic}}\right)^2+\left(\frac{G_{II}}{G_{IIc}}\right)^2=1 \tag{27}$$

where G_I and G_{II} are the energy release rates respectively in mode I and mode II, G_{Ic} and G_{IIc} are the critical energy release rates.

The total mixed-mode relative displacement δ_m can be defined as the norm of the two normal and tangential relative displacements:

$$\delta_m=\sqrt{\langle\delta_I\rangle_+^2+\delta_{II}^2} \tag{28}$$

3. Separated representation of the solution

In order to develop the PGD formulation, the full displacement field is approximated at a given time using the following separated form:

$$\mathbf{u}(x,y,z)\approx\sum_{i=1}^{n}\mathbf{F}_i(x,y)\circ\mathbf{G}_i(z)=\sum_{i=1}^{n}\begin{pmatrix}F_u^i(x,y)\times G_u^i(z)\\F_v^i(x,y)\times G_v^i(z)\\F_w^i(x,y)\times G_w^i(z)\end{pmatrix}\quad\forall(x,y,z)\in\Omega \tag{29}$$

where $\circ$ is the Hadamard product, $\mathbf{u}(x,y,z)=\begin{pmatrix}u(x,y,z)\\v(x,y,z)\\w(x,y,z)\end{pmatrix}$ is the displacement vector, $\mathbf{F}_i(x,y)=\begin{pmatrix}F_u^i(x,y)\\F_v^i(x,y)\\F_w^i(x,y)\end{pmatrix}$ are functions of the mid-plane coordinate, and $\mathbf{G}_i(z)=\begin{pmatrix}G_u^i(z)\\G_v^i(z)\\G_w^i(z)\end{pmatrix}$ are functions involving the thickness coordinate. The domain is $\Omega=\Omega_{xy}\times\Omega_z$ where Ω_{xy} and Ω_z are respectively the mid-plane and the thickness of the plate.

A same kind of separated representation is used for the velocity and the acceleration:

$$\dot{\mathbf{u}}\approx\sum_{i=1}^{n_v}\dot{\mathbf{F}}_i(x,y)\circ\dot{\mathbf{G}}_i(z)\quad\forall(x,y,z)\in\Omega \tag{30}$$

$$\ddot{\mathbf{u}}=\sum_{i=1}^{n}\ddot{\mathbf{F}}_i(x,y)\circ\ddot{\mathbf{G}}_i(z)\quad\forall(x,y,z)\in\Omega \tag{31}$$

Now the discrete problem Eq. (5) must be rewritten using these separated approximations.

3.1. Mass matrix in a separated form

To express the mass matrix, we consider the inertia term from the weak form of the equilibrium equation (Eq. (2)):

$$\iint_\Omega\rho\mathbf{u}^*\cdot\ddot{\mathbf{u}}d\Omega=\iint_\Omega\rho u^*\ddot{u}d\Omega+\iint_\Omega\rho v^*\ddot{v}d\Omega+\iint_\Omega\rho w^*\ddot{w}d\Omega \tag{32}$$

We assume for sake of simplicity that ρ is constant. It gives:

$$\iint_\Omega\rho\mathbf{u}^*\cdot\ddot{\mathbf{u}}d\Omega=\rho\sum_{\varphi=u,v,w}\iint_\Omega\varphi^*\ddot{\varphi}d\Omega \tag{33}$$

This weak formulation is valid for every $\mathbf{u}^*$ kinematically admissible. In particular, the virtual field can be chosen on the following separated form:

$$\mathbf{u}^*=\begin{pmatrix}u^*(x,y,z)\\v^*(x,y,z)\\w^*(x,y,z)\end{pmatrix}=\mathbf{R}^*(x,y)\circ\mathbf{S}^*(z)\quad\forall(x,y,z)\in\Omega \tag{34}$$

where $\mathbf{R}^*$ and $\mathbf{S}^*$ may be any kinematically admissible functions (leading to kinematically admissible $\mathbf{u}^*$) respectively on the subspace Ω_{xy} and Ω_z.

Eq. (33) can then be rewritten as:

$$\iint_\Omega \rho \mathbf{u}^* \cdot \ddot{\mathbf{u}} d\Omega = \rho \sum_{\varphi=u,v,w} \sum_{i=1}^{n} \left(\int_{\Omega_{xy}} R^*_\varphi \ddot{F}^i_\varphi dxdy \right) \left(\int_{\Omega_z} S^*_\varphi \ddot{G}^i_\varphi dz \right) \tag{35}$$

A finite element approximation can be used on the two subspace Ω_{xy} and Ω_z. After discretization, the finite element operators $\mathbf{M}_{xy}$ and $\mathbf{M}_z$ are defined such as:

$$\begin{cases} \rho \int_{\Omega_{xy}} R^*_\varphi \ddot{F}^i_\varphi dxdy & \approx \{R^*_\varphi\}^T \mathbf{M}_{xy} \{\ddot{F}^i_\varphi\} \\ \int_{\Omega_z} S^*_\varphi \ddot{G}^i_\varphi dz & \approx \{S^*_\varphi\}^T \mathbf{M}_z \{\ddot{G}^i_\varphi\} \end{cases} \tag{36}$$

where $\{\ddot{F}^i_\varphi\}, \{\ddot{G}^i_\varphi\}, \{R^*_\varphi\}$ and $\{S^*_\varphi\}$ are some column vectors containing the nodal values of $\ddot{F}^i_\varphi, \ddot{G}^i_\varphi, R^*_\varphi$ and S^*_φ respectively.

Now we want to express the global mass matrix from $\mathbf{M}_{xy}$ and $\mathbf{M}_z$. We simply define the nodal acceleration vector $\{\ddot{\mathbf{u}}\}$ by stacking the column vectors $\{\ddot{u}\}, \{\ddot{v}\}$ and $\{\ddot{w}\}$:

$$\{\ddot{\mathbf{u}}\} = \begin{bmatrix} \{\ddot{u}\} \\ \{\ddot{v}\} \\ \{\ddot{w}\} \end{bmatrix} \tag{37}$$

The nodal vector $\{\mathbf{u}^*\}$ is defined in the same way.

In the following, the Kronecker product denoted $\otimes$ will be used to build the global nodal vectors from the separated representation. This formalism has been introduced by Ammar et al. in [35]. In particular, $\{\ddot{\mathbf{u}}\}$ and $\{\mathbf{u}^*\}$ can be built with the following expressions:

$$\begin{cases} \{\ddot{\varphi}\} = \sum_{i=1}^{n} \{\ddot{F}^i_\varphi\} \otimes \{\ddot{G}^i_\varphi\} \\ \{\varphi^*\} = \{R^*_\varphi\} \otimes \{S^*_\varphi\} \end{cases} \text{for } \varphi = u, v, w \tag{38}$$

From Eqs. (35), (36), (38) and the properties of the Kronecker product, the inertia term can be rewritten as:

$$\begin{aligned} \iint_\Omega \rho \mathbf{u}^* \cdot \ddot{\mathbf{u}} d\Omega &= \sum_{\varphi=u,v,w} \sum_{i=1}^{n} \left(\{R^*_\varphi\}^T M_{xy} \{\ddot{F}^i_\varphi\} \right) \times \left(\{S^*_\varphi\}^T M_z \{\ddot{G}^i_\varphi\} \right) \\ &= \sum_{\varphi=u,v,w} \left(\{R^*_\varphi\}^T \otimes \{S^*_\varphi\}^T \right) (M_{xy} \otimes M_z) \sum_{i=1}^{n} \{\ddot{F}^i_\varphi\} \otimes \{\ddot{G}^i_\varphi\} \Big) \\ &= \sum_{\varphi=u,v,w} \{\varphi^*\}^T (M_{xy} \otimes M_z) \{\ddot{\varphi}\} \end{aligned} \tag{39}$$

The mass matrix in a separated form is deduced from Eq. (39) with a global matrix assembly on the subspace Ω_{xy} and Ω_z:

$$\begin{aligned} [\mathbf{M}] = &\begin{bmatrix} \mathbf{M}_{xy} & 0 & 0 \\ 0 & 0 & 0 \\ 0 & 0 & 0 \end{bmatrix} \otimes \begin{bmatrix} \mathbf{M}_z & 0 & 0 \\ 0 & 0 & 0 \\ 0 & 0 & 0 \end{bmatrix} + \begin{bmatrix} 0 & 0 & 0 \\ 0 & \mathbf{M}_{xy} & 0 \\ 0 & 0 & 0 \end{bmatrix} \\ &\otimes \begin{bmatrix} 0 & 0 & 0 \\ 0 & \mathbf{M}_z & 0 \\ 0 & 0 & 0 \end{bmatrix} + \begin{bmatrix} 0 & 0 & 0 \\ 0 & 0 & 0 \\ 0 & 0 & \mathbf{M}_{xy} \end{bmatrix} \otimes \begin{bmatrix} 0 & 0 & 0 \\ 0 & 0 & 0 \\ 0 & 0 & \mathbf{M}_z \end{bmatrix} \end{aligned} \tag{40}$$

The 0 in the previous equation represent null bloc matrices of the dimension equivalent to $\mathbf{M}_{xy}$ or $\mathbf{M}_z$.

3.2. Rigidity matrix in a separated form

In the weak form of the equilibrium equation, the term related to the strain energy is:

$$\mathcal{E} = \iint_\Omega \varepsilon(\mathbf{u}^*).(A\varepsilon(\mathbf{u}))d\Omega \tag{41}$$

The rigidity matrix is build with a finite element discretization of $\mathcal{E}$. The strain tensor with the small strain assumption can be expressed from the separated representation Eq. (29):

$$\boldsymbol{\varepsilon}(\mathbf{u}) = \begin{pmatrix} \partial_x u \\ \partial_y v \\ \partial_z w \\ \partial_z v + \partial_y w \\ \partial_z u + \partial_x w \\ \partial_y u + \partial_x v \end{pmatrix} = \sum_{i=1}^{n} \begin{pmatrix} \partial_x F^i_u \times G^i_u \\ \partial_y F^i_v \times G^i_v \\ F^i_w \times \partial_z G^i_w \\ F^i_v \times \partial_z G^i_v + \partial_y F^i_w \times G^i_w \\ F^i_u \times \partial_z G^i_u + \partial_x F^i_w \times G^i_w \\ \partial_y F^i_u \times G^i_u + \partial_x F^i_v \times G^i_v \end{pmatrix} \tag{42}$$

∂_x, ∂_y and ∂_z denotes respectively the derivative with respect to x, y and z. With Eq. (34), the strain tensor related to the virtual field gives:

$$\boldsymbol{\varepsilon}(\mathbf{u}^*) = \begin{pmatrix} \partial_x R^*_u \times S^*_u \\ \partial_y S^*_v \times S^*_v \\ R^*_w \times \partial_z S^*_w \\ R^*_v \times \partial_z S^*_v + \partial_y R^*_w \times S^*_w \\ R^*_u \times \partial_z S^*_u + \partial_x R^*_w \times S^*_w \\ \partial_y R^*_u \times S^*_u + \partial_x R^*_v \times S^*_v \end{pmatrix} \tag{43}$$

$\mathcal{E}$ can be developed in a sum of simple integrals:

$$\mathcal{E} = \sum_{i=1}^{6} \sum_{j=1}^{6} \iint_\Omega A_{ij} \varepsilon_i(\mathbf{u}^*) \varepsilon_j(\mathbf{u}) d\Omega \tag{44}$$

If we assume that A_{ij} can be written in a separated form, i.e. $A_{ij}(x,y,z) = \sum_k A^{xy}_{ijk}(x,y) \times A^z_{ijk}(z)$, and using Eq. (42)–(44), we can write $\mathcal{E}$ as a sum of products of integrals defined on the subspace Ω_{xy} by integrals defined on Ω_z. With a finite element approximation on each subspace Ω_{xy} and Ω_z, we can build some finite element operators $\mathbf{K}^p_{xy}$ and $\mathbf{K}^p_z$ such as:

$$\begin{aligned} \mathcal{E} &= \sum_{p=1}^{m} \sum_{i=1}^{n} \left(\{\mathbf{R}^*\}^T K^p_{xy} \{\mathbf{F}_i\} \right) \times \left(\{\mathbf{S}^*\}^T K^p_z \{\mathbf{G}_i\} \right) \\ &= \sum_{p=1}^{m} \left(\{\mathbf{R}^*\}^T \otimes \{\mathbf{S}^*\}^T \right) \left(K^p_{xy} \otimes K^p_z \right) \times \sum_{i=1}^{n} \{\ddot{\mathbf{F}}_i\} \otimes \{\ddot{\mathbf{G}}_i\} \Big) \\ &= \sum_{p=1}^{m} \{\mathbf{u}^*\}^T \left(K^p_{xy} \otimes K^p_z \right) \{\mathbf{u}\} \end{aligned} \tag{45}$$

m depends on the non zero terms of $\mathbf{A}$. $\{\mathbf{R}^*\}$, $\{\mathbf{S}^*\}$, $\{\mathbf{F}_i\}$and $\{\mathbf{G}_i\}$ contain respectively the nodal values of $\mathbf{R}^*$, $\mathbf{S}^*$, $\mathbf{F}_i$ and $\mathbf{G}_i$. Finally, the finite element rigidity matrix is:

$$[\mathbf{K}] = \sum_{p=1}^{m} \mathbf{K}^p_{xy} \otimes \mathbf{K}^p_z \tag{46}$$

3.3. Cohesive zone

The introduction of the cohesive zones in the separated representation of the rigidity matrix have been widely described in [36] for simple static problems.

In the presence of a cohesive surface Γ_{coh} the weak form Eq. (2) becomes:

$$\iint_\Omega \rho \mathbf{u}^* . \ddot{\mathbf{u}} d\Omega + \iint_\Omega \varepsilon(\mathbf{u}^*).(A\varepsilon(\mathbf{u}))d\Omega + \int_{\Gamma_{coh}} \mathbf{T}_{coh} \boldsymbol{\delta}^* d\Gamma = \int_\Gamma \mathbf{T}_{ext} \mathbf{u}^* d\Gamma \tag{47}$$

where $\boldsymbol{\delta}^*$ is the virtual separation vector and $\mathbf{T}_{coh}$ is the cohesive stress vector. The term $\int_{\Gamma_{coh}} \mathbf{T}_{coh}\boldsymbol{\delta}^* d\Gamma$ represent the virtual work related to the cohesive surface.

Two cases are treated in the following:

1. The cohesive surface Γ_{coh} is parallel to the mid-plane surface of the plate (delamination) that have already been described in [36].
2. The cohesive surface Γ_{coh} is normal to the mid-plane surface of the plate (ply failure).

3.3.1. Cohesive surface parallel to the mid-plane surface

As said, this case have been widely described in [36]. In this paragraph, we briefly recall the main contribution of our former article. This case, the cohesive surface is normal to the z axis so that $\Gamma_{coh} \equiv \Omega_{xy}$. With the Crisfield model, the relation between the stress vector $\mathbf{T}_{coh}$ and the relative displacement vector $\boldsymbol{\delta}$ is given by:

$$\mathbf{T}_{coh} = \begin{pmatrix} \sigma_{xz} \\ \sigma_{yz} \\ \sigma_{zz} \end{pmatrix} = \begin{pmatrix} \lambda K_{II}\delta_x \\ \lambda K_{II}\delta_y \\ \lambda K_I \delta_z \end{pmatrix} \tag{48}$$

where the relative displacement reads:

$$\boldsymbol{\delta} = \begin{pmatrix} \delta_x \\ \delta_y \\ \delta_z \end{pmatrix} = \begin{pmatrix} u(x,y,z^+) - u(x,y,z^-) \\ v(x,y,z^+) - v(x,y,z^-) \\ w(x,y,z^+) - w(x,y,z^-) \end{pmatrix} \tag{49}$$

The superscripts + and − in exponent indicate the two sides of the cohesive zone. The initial positions of the two faces of the cohesive zone are defined by their coordinates on Ω_z denoted z^+ and z^- for all $x, y \in \Omega_{xy}$. After discretization, z^+ and z^- define the coordinates of two nodes on Ω_z that are in general at the same initial position.

In pure modes (mode I or II), the values of λ is computed from Eq. (24).

$$\lambda = \begin{cases} 1 & \delta_j < \delta_c^j \\ (1 - d_j) & \delta_c^j \leqslant \delta_j < \delta_m^j, \quad j = I, II \\ 0 & \delta_j \geqslant \delta_m^j \end{cases} \tag{50}$$

In this case, $\delta_I = \delta_z$ and $\delta_{II} = \sqrt{\delta_x^2 + \delta_y^2}$.

In mixed mode (mode I and II), λ is computed from the relations given in Section 2.4.

To use the Proper Generalized Decomposition, the relative displacement vector must be expressed in a separated form. This expression is deduced from Eqs. (29) and (49):

$$\begin{cases} \delta_x = \sum_{i=1}^{n} F_u^i(x,y)\left(G_u^i(z^+) - G_u^i(z^-)\right) \\ \delta_y = \sum_{i=1}^{n} F_v^i(x,y)\left(G_v^i(z^+) - G_v^i(z^-)\right) \\ \delta_z = \sum_{i=1}^{n} F_w^i(x,y)\left(G_w^i(z^+) - G_w^i(z^-)\right) \end{cases} \tag{51}$$

The virtual separation $\boldsymbol{\delta}^*$ can also be expressed as:

$$\begin{cases} \delta_x^* = R_u^*(x,y)\left(S_u^*(z^+) - S_u^*(z^-)\right) \\ \delta_y^* = R_v^*(x,y)\left(S_v^*(z^+) - S_v^*(z^-)\right) \\ \delta_z^* = R_w^*(x,y)\left(S_w^*(z^+) - S_w^*(z^-)\right) \end{cases} \tag{52}$$

The term related to the cohesive zone in the weak formulation Eq. (47) becomes with Eqs. (48), (51) and (52):

$$\begin{aligned} \int_{\Gamma_{coh}} \mathbf{T}_{coh}\boldsymbol{\delta}^* d\Gamma = \sum_{i=1}^{n} \Bigg[& \left(\int_{\Omega_{xy}} \lambda K_{II} R_u^*(x,y) F_u^i(x,y)\, dxdy \right) \times \left(S_u^*(z^+) - S_u^*(z^-)\right) \\ & \times \left(G_u^i(z^+) - G_u^i(z^-)\right) \left(\int_{\Omega_{xy}} \lambda K_{II} R_v^*(x,y) F_v^i(x,y)\, dxdy \right) \\ & \times \left(S_v^*(z^+) - S_v^*(z^-)\right) \left(G_v^i(z^+) - G_v^i(z^-)\right) \\ & \times \left(\int_{\Omega_{xy}} \lambda K_I R_w^*(x,y) F_w^i(x,y)\, dxdy \right) \times \left(S_w^*(z^+) - S_w^*(z^-)\right) \\ & \times \left(G_w^i(z^+) - G_w^i(z^-)\right) \Bigg] \end{aligned} \tag{53}$$

Each integral over Ω_{xy} gives a finite element operator after a finite element assembly. The parts related to z are already discrete and therefore easy to assemble in a global matrix. The finite element operator related to the cohesive zone can then be built under a separated form and added to the rigidity matrix. In general, 3 terms are added to the sum defined in Eq. (46).

3.3.2. Cohesive surface normal to the mid-plane surface

In this case, the cohesive surface is normal to the plane $\Omega_{xy} \equiv (x,y)$. We assume for sake of clarity and without loss of generality that the cohesive surface is normal to the x axis, ie $\Gamma_{coh} \equiv \Omega_{yz} = (y,z)$. The relation between the stress vector $\mathbf{T}_{coh}$ and the relative displacement vector $\boldsymbol{\delta}$ is then given by:

$$\mathbf{T}_{coh} = \begin{pmatrix} \sigma_{xx} \\ \sigma_{xy} \\ \sigma_{xz} \end{pmatrix} = \begin{pmatrix} \lambda K_I \delta_x \\ \lambda K_{II}\delta_y \\ \lambda K_{II}\delta_z \end{pmatrix} \tag{54}$$

The initial positions of the two faces of the cohesive zone are defined by their coordinates on the x axis denoted x^+ and x^- for all $y, z \in \Omega_{yz}$. The relative displacement can then be written as:

$$\begin{pmatrix} \delta_x \\ \delta_y \\ \delta_z \end{pmatrix} = \begin{pmatrix} u(x^+,y,z) - u(x^-,y,z) \\ v(x^+,y,z) - v(x^-,y,z) \\ w(x^+,y,z) - w(x^-,y,z) \end{pmatrix} \tag{55}$$

The symbols + and − indicate the two sides of the cohesive surface. Using 29, the relative displacement reads:

$$\begin{cases} \delta_x = \sum_{i=1}^{n} \left(F_u^i(x^+,y) - F_u^i(x^-,y)\right) G_u^i(z) \\ \delta_y = \sum_{i=1}^{n} \left(F_v^i(x^+,y) - F_v^i(x^-,y)\right) G_v^i(z) \\ \delta_z = \sum_{i=1}^{n} \left(F_w^i(x^+,y) - F_w^i(x^-,y)\right) G_w^i(z) \end{cases} \tag{56}$$

And with Eq. (34) the virtual separation δ^* can be written as:

$$\begin{cases} \delta_x^* = \left(R_u^*(x^+,y) - R_u^*(x^-,y)\right) S_u^*(z) \\ \delta_y^* = \left(R_v^*(x^+,y) - R_v^*(x^-,y)\right) S_v^*(z) \\ \delta_z^* = \left(R_w^*(x^+,y) - R_w^*(x^-,y)\right) S_w^*(z) \end{cases} \tag{57}$$

Finally, the term related to the cohesive zone in the weak formulation Eq. (47) becomes:

$$\begin{aligned} \int_{\Gamma_{coh}} \mathbf{T}_{coh}\boldsymbol{\delta}^* d\Gamma = \sum_{i=1}^{n} \Bigg[& \left(\int_{\Omega_y} \lambda K_I \left(R_u^*(x^+,y) - R_u^*(x^-,y)\right) \left(F_u^i(x^+,y) - F_u^i(x^-,y)\right) dy \right) \\ & \times \left(\int_{\Omega_z} S_u^*(z) G_u^i(z)\, dz \right) \left(\int_{\Omega_y} \lambda K_{II} \left(R_v^*(x^+,y) - R_v^*(x^-,y)\right) \left(F_v^i(x^+,y) - F_v^i(x^-,y)\right) dy \right) \\ & \times \left(\int_{\Omega_z} S_v^*(z) G_v^i(z)\, dz \right) \left(\int_{\Omega_y} \lambda K_{II} \left(R_w^*(x^+,y) - R_w^*(x^-,y)\right) \left(F_w^i(x^+,y) - F_w^i(x^-,y)\right) dy \right) \\ & \times \left(\int_{\Omega_z} S_w^*(z) G_w^i(z)\, dz \right) \Bigg] \end{aligned} \tag{58}$$

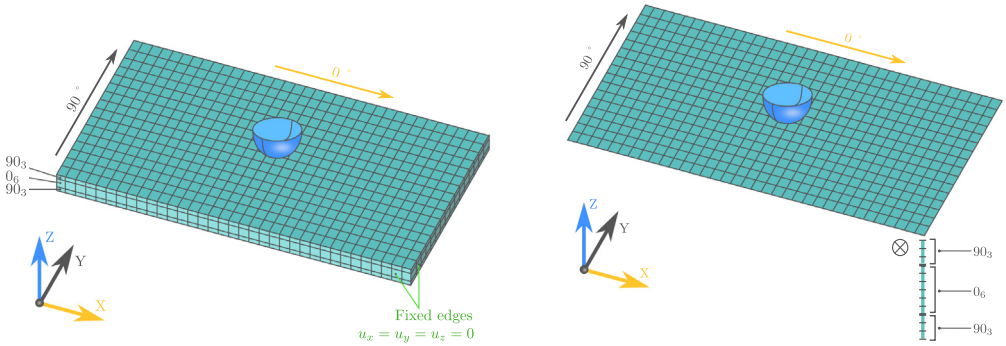

Fig. 5. Numerical models used for impact analysis.

Table 1
Material properties of the laminate and impactor properties.

Laminated plate	$E_L = 157,380$ MPa; $E_T = 11,873$ MPa $G_{LT} = G_{TT} = 5051$ MPa $\nu_{LT} = \nu_{TT} = 0.31$
Impactor	$E_i = 207$ GPa; $\nu_i = 0.30$ $\rho_i = 7800$ kg/m^3; $R_i = 12.5$ mm

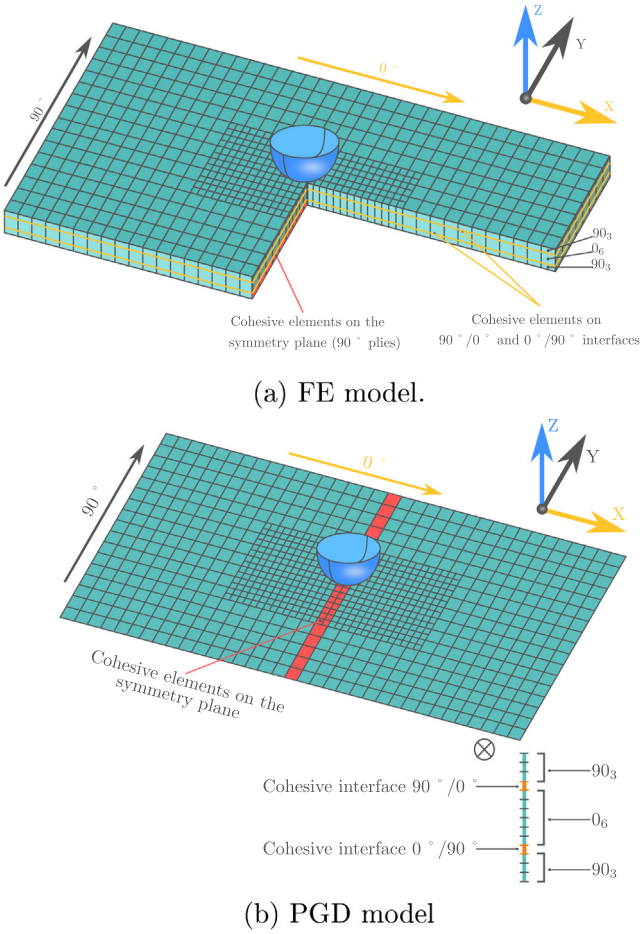

Fig. 6. Location of cohesive elements.

Each integral over Ω_z gives a finite element operator after a finite element assembly. Some 2D cohesive elements can also be assembled in a global operator on Ω_{xy}. Finally, the finite element operator related to the cohesive zone can be built under a separated form and added to the rigidity matrix in the sum defined in Eq. (46).

3.4. Proper generalized decomposition

In this work, the time is treated incrementally with the Newmark's scheme. A Proper Generalized Decomposition is required at each time step to build the solution.

Firstly, the dynamical system at a time t (Eq. (10)) must be rewritten in a separated form. This is trivial when we get the discretized operators (mass and rigidity matrix) in a separated form. The effective stiffness matrix can then be expressed as:

$$[\mathbf{K}^*] = \left[[\mathbf{K}] + \frac{1}{\beta(\Delta t)^2}[\mathbf{M}]\right] = \sum_{p=1}^{m} \mathbf{K}_{xy}^{*p} \otimes \mathbf{K}_z^{*p} \tag{59}$$

The force matrix at a time $t + \Delta t$ must also be written in the following separated form:

$$\{F_{t+\Delta t}^*\} = \sum_{p=1}^{m_f} \{f_{xy}^{*p}\} \otimes \{f_z^{*p}\} \tag{60}$$

The Galerkin method with the classical greedy algorithm is used to build the Proper Generalized Decomposition. The method is briefly described in the following.

We consider the weak form of the dynamical equation Eq. (10):

$$\{\mathbf{u}^*\}^T[\mathbf{K}^*]\{\mathbf{u}\} = \{\mathbf{u}^*\}^T\{F_{t+\Delta t}^*\} \qquad \forall\{\mathbf{u}^*\} \tag{61}$$

The n first terms of the separated approximation of the solution are assumed known. Then we want to enrich the solution, ie to add a new term $n+1$ such as:

$$\{\mathbf{u}\} = \sum_{i=1}^{n} \{\mathbf{F}_i\} \otimes \{\mathbf{G}_i\} + \{\mathbf{F}_{n+1}\} \otimes \{\mathbf{G}_{n+1}\} \tag{62}$$

Of course, at the beginning when $n = 0$ nothing is known a priori. The problem consists in finding $\{\mathbf{F}_{n+1}\}$ and $\{\mathbf{G}_{n+1}\}$. This is a non-linear problem that needs to be linearized. To solve it, an alternate direction strategy is used:

Table 2
Cohesive properties.

Cohesive properties	$K_I = 1.10^4$ N/mm^3; $K_{II} = 5.10^4$ N/mm^3 $\sigma_c = 60$ MPa; $\tau_c = 139$ MPa $G_{Ic} = 0.3$ N/mm; $G_{IIc} = 1.6$ N/mm

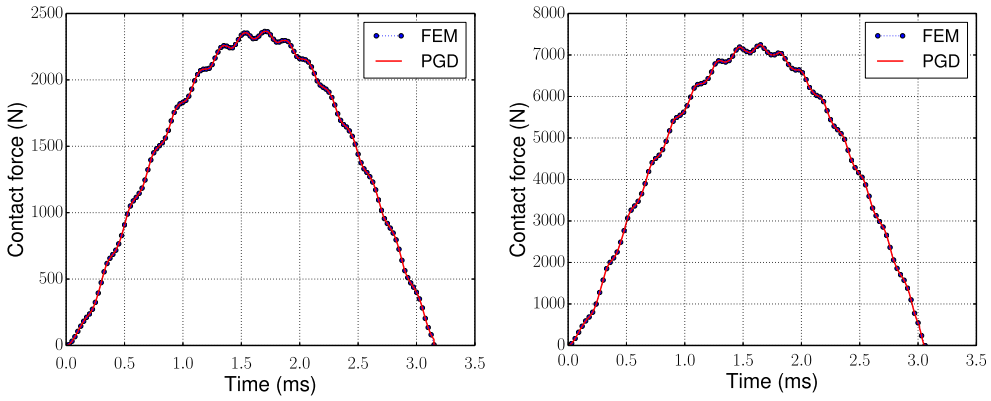

Fig. 7. Comparison of contact force-time history.

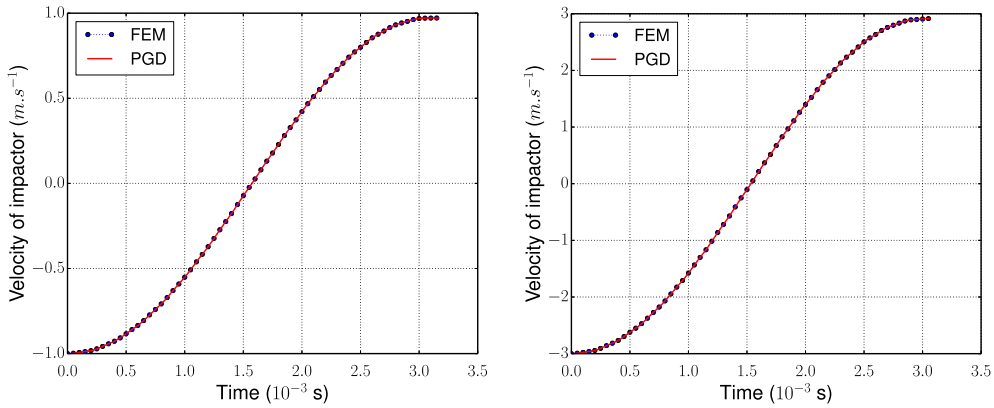

Fig. 8. Velocity of the impactor.

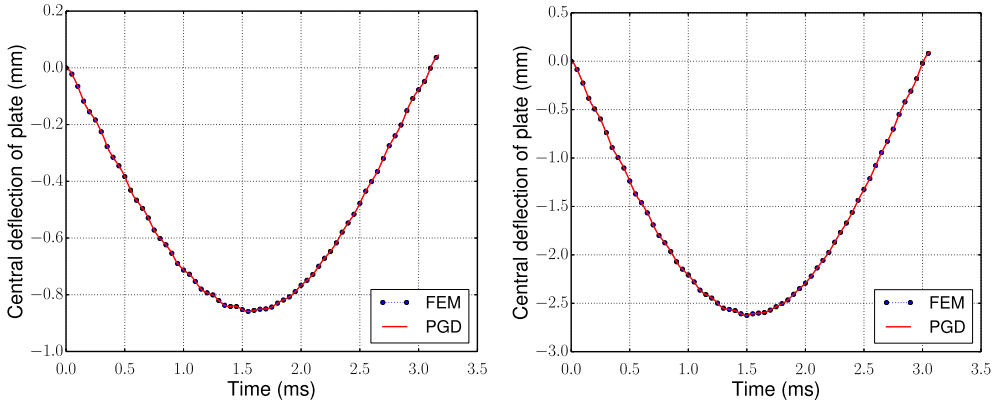

Fig. 9. Comparison of plate central displacement-time history.

1. Initialize the values for $\{\mathbf{F}_{n+1}\}$ and $\{\mathbf{G}_{n+1}\}$ to a random values.
2. Update $\{\mathbf{F}_{n+1}\}$ knowing $\{\mathbf{G}_{n+1}\}$.
3. Update $\{\mathbf{G}_{n+1}\}$ knowing $\{\mathbf{F}_{n+1}\}$.
4. Check the convergence, for instance in comparing two successive values of $\{\mathbf{F}_{n+1}\}$ and $\{\mathbf{G}_{n+1}\}$.
5. If not converged, return to 2.

Only step 2 is described now, step 3 being very similar.

$\{\mathbf{F}_i\}$ and $\{\mathbf{G}_i\}$ are known for $i = 1 \ldots N$. $\{\mathbf{G}_{n+1}\}$ is also known and we want to compute$\{\mathbf{F}_{n+1}\}$. Therefore the virtual displacement can be written as:

$$\{\mathbf{u}^*\} = \{\mathbf{F}^*_{n+1}\} \otimes \{\mathbf{G}_{n+1}\} \tag{63}$$

With Eqs. (62) and (63) the weak form of the dynamical equation Eq. (61) can be expressed as:

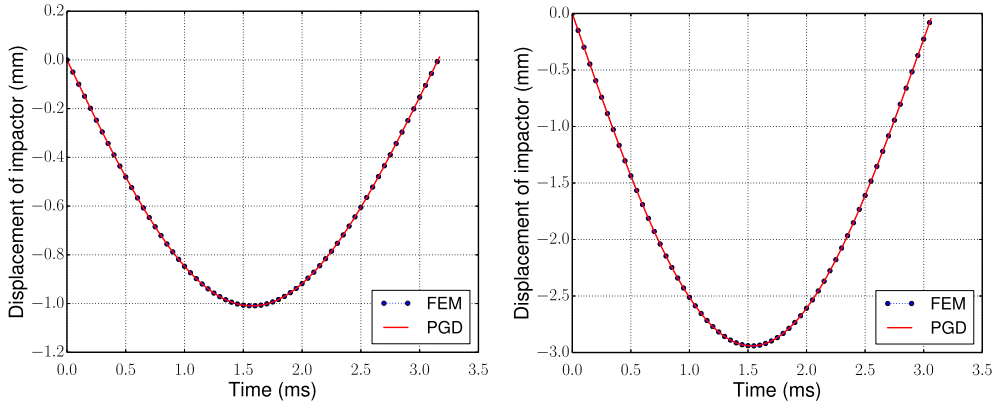

Fig. 10. Displacement of the impactor.

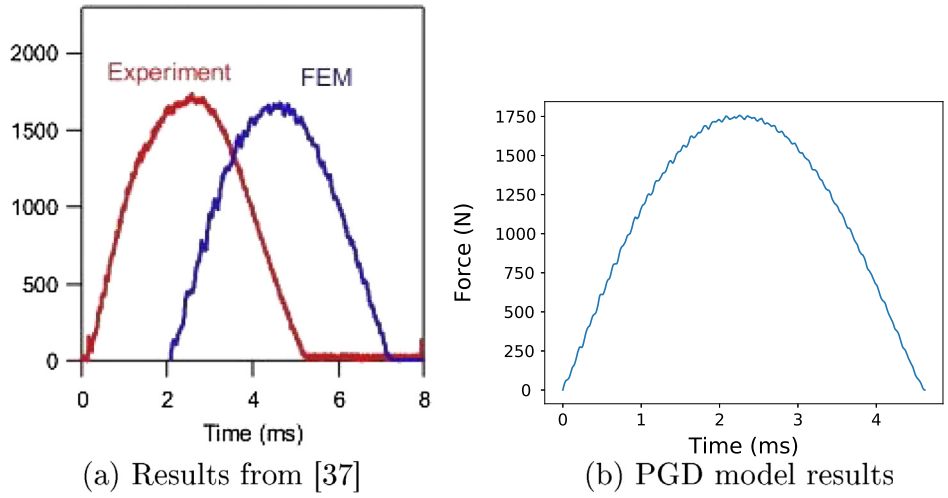

Fig. 11. Force history for an impact of 1.5 J compared with experimental results.

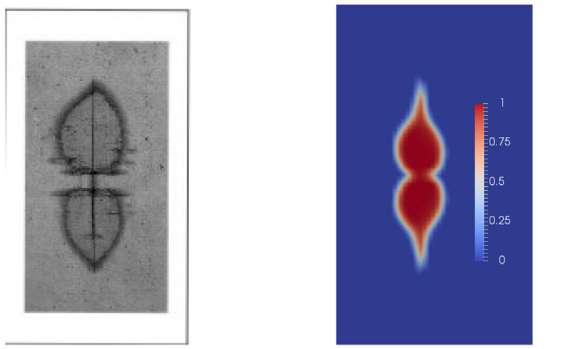

Fig. 12. Delamination areas for the lower interface 0°/90° of the laminate $[90_3/0_3]$ s subjected to impact energy 1.5 J.

$$\left(\{\mathbf{F}^*_{n+1}\}\otimes\{\mathbf{G}_{n+1}\}\right)^T[\mathbf{K}^*](\{\mathbf{F}_{n+1}\}\otimes\{\mathbf{G}_{n+1}\})$$
$$= \left(\{\mathbf{F}^*_{n+1}\}\otimes\{\mathbf{G}_{n+1}\}\right)\{F^*_{t+\Delta t}\} - \left(\{\mathbf{F}^*_{n+1}\}\otimes\{\mathbf{G}_{n+1}\}\right)^T[\mathbf{K}^*]\ \sum_{i=1}^{n}\{\mathbf{F}_i\}\otimes\{\mathbf{G}_i\}\Big) \tag{64}$$

By splitting $[\mathbf{K}^*]$ and $\{F^*_{t+\Delta t}\}$ with Eqs. (59) and (60) and using the properties of the Kronecker product we get:

$$\sum_{p=1}^{m}\mathbf{K}^{*p}_{xy}\{\mathbf{F}_{n+1}\}\times\left(\{\mathbf{G}_{n+1}\}^T\mathbf{K}^{*p}_{z}\{\mathbf{G}_{n+1}\}\right)$$
$$= \sum_{p=1}^{m_f}\{f^{*p}_{xy}\}\times\left(\{\mathbf{G}_{n+1}\}^T\{f^{*p}_{z}\}\right) - \sum_{i=1}^{n}\sum_{p=1}^{m}\mathbf{K}^{*p}_{xy}\{\mathbf{F}_i\}\times\left(\{\mathbf{G}_i\}^T\mathbf{K}^{*p}_{z}\{\mathbf{G}_i\}\right) \tag{65}$$

Eq. (65) is a simple linear system from which $\{\mathbf{F}_{n+1}\}$ can be computed.

Once $\{\mathbf{u}_{t+\Delta t}\}$ have been computed on a separated form, $\{\dot{\mathbf{u}}_{t+\Delta t}\}$ and $\{\ddot{\mathbf{u}}_{t+\Delta t}\}$ can be computed from Eqs. (8) and (9).

Remark. The number of terms in the separated representation of $\{F^*_{t+\Delta t}\}$ is generally very high due to the sum in Eq. (60). This strongly penalizes the computational time. To overcome this problem, the separated representations of $\{F^*_{t+\Delta t}\}$ may be recomputed using a Singular Value Decomposition or using a PGD with the identity operator, ie by solving with the PGD algorithm the equation:

$$\{F^*_{t+\Delta t}\}_{new} = \{F^*_{t+\Delta t}\}_{old}$$
$$= \{F_{t+\Delta t}\} + [\mathbf{M}]\left\{\frac{1}{\beta(\Delta t)^2}\{\mathbf{u}_t\} + \frac{1}{\beta(\Delta t)}\{\dot{\mathbf{u}}_t\} + (\frac{1}{2\beta}-1)\{\ddot{\mathbf{u}}_t\}\right\} \tag{66}$$

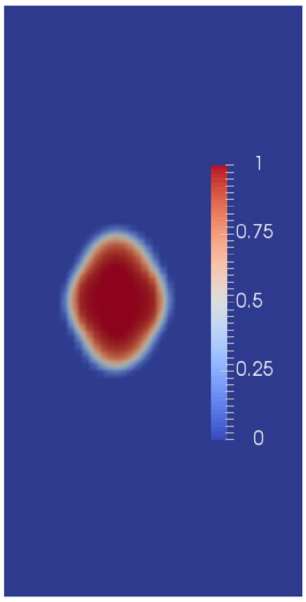

Fig. 13. Delamination areas for the upper interface $90^\circ/0^\circ$ of the laminate $[90_3/0_3]$ s subjected to impact energy 1.5 J.

4. Numerical simulation

4.1. Geometrical modeling and Boundary conditions

In our previous works [36], we have demonstrated that the PGD can be used as an alternative to overcome the computational drawbacks of FEM such as the rapid increase in the number of degrees of freedom, the large computational time, and the storage limitation. In this work, the predictive capabilities of the PGD approach are evaluated by simulating the low velocity impact response of cross-ply laminates. The impact response analysis is also performed using a standard FE approach.

We consider a rectangular plate $60 \times 40 \times 3$ mm made of unidirectional carbon/epoxy material, with stacking sequence $[90_3/0_3]$ s. The cross-ply laminate is assumed to be clamped along all the four edges and impacted at the center by a 12.7 mm diameter aluminum sphere. An initial velocity V_0 is applied to the impactor. All the nodes of the plate edge are fixed in all directions (x, y, z) to simulate the experimental clamped conditions. The main advantage of the PGD approach in comparison with the basic FEM approach is the reduction of the computational time. To do that, the 3D mesh is separated into 2D and 1D meshes as represented in Fig. 5. The boundary conditions are also shown in the same figure. The material properties used in the simulations are listed in Table 1 where the subscript L and T denotes respectively the direction of fibers and the transverse direction.

4.2. Results

In the PGD model, the smallest element size in the impact zone is 0.3×0.3 mm. The size of elements was selected by sensitivity analysis in terms of convergence, structural response and damage propagation. The sensitivity analysis showed that the PGD model is less sensitive to mesh size than the FE model. The fine mesh region on the laminate plane is 40 mm $\times$ 20 mm, as shown in Fig. 6. Each element layer represents one lamina ply.

As discussed previously, under low-velocity impact, damage is initiated by matrix cracking in the lowest ply of the laminate, which create delaminations at interfaces between plies with different fiber orientations. Based on this analysis and as done in [37], two rows of vertical cohesive elements are placed on the symmetry plane parallel to the 90° direction to simulate the initiation and growth of the major intralaminar matrix crack (bending crack), typically developing along the fiber direction in the lower block of layers (Fig. 6). To simulate the initiation and propagation of the delamination, cohesive elements are also inserted at the interfaces between layers with different fiber orientations ($0^\circ/90^\circ$ and $90^\circ/0^\circ$ intarfaces). The properties of the cohesive elements are presented in Table 2. The cohesive elements share nodes with the solid elements and have zero thickness.

The PGD discretization allows a reduction of the number of interface elements in comparison with the FEM discretization, which minimizes modeling complexity.

The impact simulation described previously were performed with two different initial impact velocities: 1 m s^{-1} and 3 m s^{-1}. The mass of the impactor is equal to 2.3 kg. The time step used for the implicit newmark algorithm is 10^{-4} ms. The evolution of the impact force for the two initial impact velocities obtained with the PGD and the FEM are depicted in Fig. 7. The PGD and the FEM gives very similar results. Fig. 8 shows the velocity of the impactor-time history. In Figs. 9 and 10 the deflexion of the plate at the contact point and the displacement of the impactor versus time are shown. All the results shows a good agreement between FEM and PGD. The PGD is adapted to perform impact simulation using an incremental implicit newmark scheme.

4.3. Comparison with experimental results

The simulation have also been launched using the parameters corresponding to the experimental configuration developed by Aymerich et al. in [37]. This test case concerns carbon/epoxy composite plates with a fiber volume fraction $V_f = 50\%$. and the material properties have been set accordingly ($E_L = 127,000$ MPa, $E_T = 9370$ MPa, $G_{LT} = 3900$ MPa, $G_{TT} = 3358$ MPa, $\nu_{LT} = 0.31$, $\nu_{TT} = 0.39$). The impactor is the same as in previous section (2.3 kg) and the cohesive properties proposed in [37] have been used.

We can see in Fig. 11 that the resulting force history for a impact energy of 1.5 J (impactor initial velocity $\approx$ 1.14 m/s) is quite coherent with the experimental one (maximal force around 1750 N at t = 2.2 ms). The damage shapes of the lower interface $0^\circ/90^\circ$ and the upper interface $0^\circ/90^\circ$ are similar to the experimental damage given by Ayemrich et al. (Fig.).

The delamination shapes obtained from the PGD simulation at the upper and lower interfaces are shown in Figs. 12 and in 13 using the same scale. The length and width of the delaminated area are respectively 21.4 mm and 6.8 mm for the experimental results and 20.5 mm and 6 mm for the PGD model. The propose model is thus satisfactory to give and estimation of the shape of delaminated area.

5. Conclusion and perspectives

In this article, we have shown the ability of the PGD to predict the impact response of a $[90_3/0_3]_s$ cross-ply laminate under a low velocity impact. The PGD have been implemented in conjunction with CZM to represent delamination and matrix cracking. A close agreement is observed between the PGD and the FEM. The two methods have been compared with regard to the contact force, the damage variables, the displacement and velocity of the impactor. In addition, the method have been compared with experimental results and shows a good ability to predict the force history and delamination shape.

However, the method may be improved in some future works:

- For this example, the computational cost of the PGD remains of the same order of magnitude as the one of the FEM. A significant gain is expected for more complex simulations with more degrees of freedom in the thickness. Some improvement in the algorithm that build the separated representation should be developed in order to increase the computational efficiency of the proposed strategy.
- The proposed model only accounts for delamination and localized matrix crack. This is not always sufficient to study complex damage in industrial structures. Therefore, the model should be improved to consider the different damage types and the interaction between them. In particular the use of the extended finite element method (XFEM) should be investigated to model damages without modifying the mesh.
- The proposed approach developed in plate structures could be extended to shell structures with the strategy proposed in [12].

References

[1] Ladeveze P, Nouy A. On a multiscale computational strategy with time and space homogenization for structural mechanics. Comput Meth Appl Mech Eng 2003;192(28–30):3061–87.
[2] Ladeveze P, Passieux J, Neron D. The latin multiscale computational method and the proper generalized decomposition. Comput Meth Appl Mech Eng 2010;199(21–22):1287–96.
[3] Ammar A, Mokdad B, Chinesta F, Keunings R. A new family of solvers for some classes of multidimensional partial differential equations encountered in kinetic theory modeling of complex fluids. J Non-Newt Fluid Mech 2006;139(3):153–76.
[4] Ammar A, Mokdad B, Chinesta F, Keunings R. A new family of solvers for some classes of multidimensional partial differential equations encountered in kinetic theory modelling of complex fluids: Part ii: Transient simulation using space-time separated representations. J Non-Newt Fluid Mech 2007;144(2–3):98–121.
[5] Ammar A, Chinesta F, Cueto E, Doblaré M. Proper generalized decomposition of time-multiscale models. Int J Numer Meth Eng 2012;90(5):569–96.
[6] Chinesta F, Ammar A, Cueto E. On the use of proper generalized decompositions for solving the multidimensional chemical master equation. Euro J Comput Mech 2010;19(1):53–64.
[7] Chinesta F, Ammar A, Falco A, Laso M. On the reduction of stochastic kinetic theory models of complex fluids. Model Simul Mater Sci Eng 2007;15(6):639.
[8] Pruliere E, Ferec J, Chinesta F, Ammar A. An efficient reduced simulation of residual stresses in composite forming processes. Int J Mater Form 2010;3(2):1339–50.
[9] Nouy A. Generalized spectral decomposition method for solving stochastic finite element equations: invariant subspace problem and dedicated algorithms. Comput Meth Appl Mech Eng 2008;197(51–52):4718–36.
[10] Nouy A, Maitre OPL. Generalized spectral decomposition for stochastic nonlinear problems. J Comput Phys 2009;228(1):202–35.
[11] Bognet B, Bordeu F, Chinesta F, Leygue A, Poitou A. Advanced simulation of models defined in plate geometries: 3d solutions with 2d computational complexity. Comput Meth Appl Mech Eng 2012;201–204:1–12.
[12] Pruliere E. 3d simulation of laminated shell structures using the proper generalized decomposition. Compos Struct 2014;117:373–81.
[13] Vidal P, Gallimard L, Polit O. Composite beam finite element based on the proper generalized decomposition. Comput Struct 2012;102–103:76–86.
[14] Vidal P, Gallimard L, Polit O. Shell finite element based on the proper generalized decomposition for the modeling of cylindrical composite structures. Comput Struct 2014;132:1–11.
[15] Choi H, Downs R, Chang F. A new approach toward understanding damage mechanisms and mechanics of laminate composites due to low-velocity impact: Part i – Experiments. J Compos Mater 1991;25:992–1011.
[16] Choi H, Downs R, Chang F. A new approach toward understanding damage mechanisms and mechanics of laminate composites due to low-velocity impact: Part ii – Analysis. J Compos Mater 1991;25:1011–38.
[17] Joshi SP, Sun CT. Impact-induced fracture in a quasi-isotropic laminate. J Compos Technol Res 1987;9(2):40–6.
[18] Poon C, Bellinger RGN, Xiong Y. Edge delamination of composite laminates. In: The 9th international conference on composite materials; 1993. p. 12.1–12.13.
[19] Majeed O. Numerical modelling of transverse impact on composite coupons. Ph.D. thesis. Carleton University - Ottawa Canada.
[20] Fuoss E. Effects of stacking sequence on the impact resistance of composite laminates. Ph.D. thesis. Carleton University - Ottawa Canada.
[21] Lin H, Lee Y. Impact-induced fracture in laminated plates and shells. J Compos Mater 1990;24:1179–99.
[22] Newmark NM. A method of computation for structural dynamics. J Eng Mech Div 85(EM3).
[23] Trousset E. Prévision des dommages d'impact basse vitesse et basse énergie dans les composites à matrice organique stratifiés. Ph.D. thesis. École Nationale Supérieure d'Arts et Métiers - Centre d'Angers.
[24] Tan TM, Sun CT. Use of statical indentation law in the impact analysis of laminated composite plates. J Compos Mater 1985;52:6–12.
[25] Yigit AS, Christoforou AP. Impact dynamics of composite beams. Compos Struct 1995;32:187–95.
[26] Yigit AS, Christoforou AP. Characterization of impact in composite plates. Compos Struct 1998;43:15–24.
[27] Roy T, Chakraborty D. Delamination in {FRP} laminates with holes under transverse impact. Mater Des 2008;29(1):124–32.
[28] Choi IH, Lim CH. Low-velocity impact analysis of composite laminates using linearized contact law. Compos Struct 2004;66(1–4):125–32.
[29] Li DH, Liu Y, Zhang X. Low-velocity impact responses of the stiffened composite laminated plates based on the progressive failure model and the layerwise/solid-elements method. Compos Struct 2014;110:249–75.
[30] Li D. Delamination and transverse crack growth prediction for laminated composite plates and shells. Comput Struct 2016;177:39–55.
[31] Alfano G, Crisfield MA. Finite element interface models for the delamination analysis of laminated composites: mechanical and computational issues. Int J Numer Meth Eng 2001;50(7):1701–36.
[32] Chen J, Crisfield M, Kinloch AJ, Busso EP, Matthews FL, Qiu Y. Predicting progressive delamination of composite material specimens via interface elements. Mech Compos Mater Struct 1999;6(4):301–17.
[33] Turon PCA, Davila CG, Costa J. An engineering solution for mesh size effects in the simulation of delamination using cohesive zone models. Eng Fract Mech 2007;74(10):1665–82.
[34] Lee MJ, Cho TM, Kim WS, Lee BC, Lee JJ. Determination of cohesive parameters for a mixed-mode cohesive zone model. Int J Adhes Adhes 2010;30(5):322–8.
[35] Ammar A, Chinesta F, Falcó A. On the convergence of a greedy rank-one update algorithm for a class of linear systems. Arch Comput Meth Eng 2010;17(4):473–86.
[36] Metoui S, Pruliere E, Ammar A, Dau F, Iordanoff I. The proper generalized decomposition for the simulation of delamination using cohesive zone model. Int J Numer Meth Eng 2014;99(13):1000–22.
[37] Aymerich F, Dore F, Priolo P. Simulation of multiple delaminations in impacted cross-ply laminates using a finite element model based on cohesive interface elements. Compos Sci Technol 2009;69(11–12):1699–709.